Journal of High School Science

Descriptive imaging analysis of Glioblastoma-associated vascular morphology in a single murine brain slice

Kim C

Submitted: December 11, 2025, Revised: version 1, February 18, 2026, version 2, April 10, 2026, version 3, April 17, 2026, version 4, April 18, 2026, version 5, April 18, 2026, version 6, April 18, 2026
Accepted: April 20, 2026

Abstract

Glioblastoma is characterized by pronounced spatial heterogeneity in vascular structure, which is often assessed using imaging-based approaches. In this study, we present a descriptive analysis of vascular morphology within a single murine brain section containing a tumor region, using confocal microscopy and image-based quantification. A single brain slice (n = 1) was selected for detailed analysis, and spatially resolved measurements were obtained across contralateral, peritumoral, and intratumoral regions using tile-based segmentation and processing workflows implemented in Fiji (ImageJ). Across this specimen, regional variations in vascular-associated metrics, including the CD31-positive area and skeletonized network features, were observed. The intratumoral region exhibited higher apparent vascular density and altered structural characteristics relative to the surrounding regions, while the peritumoral zone showed intermediate patterns. These observations are consistent with previously reported spatial heterogeneity in tumor-associated vasculature, although no statistical inference can be made due to the single-sample design. This work is intended as an exploratory and methodological case study demonstrating a reproducible pipeline for spatial quantification of vascular features in confocal brain images. The findings are descriptive and hypothesis-generating, highlighting patterns that may inform future studies with appropriate biological replication and statistical power.

Keywords

Glioblastoma, Brain, Cerebral vasculature, Branches, Junctions, Angiogenesis, Neovascularization inside tumor, Contralateral hemisphere, Peritumoral brain zone, Methodological case study

Chaeun Kim, Korea International School Jeju Campus, 8 Global Edu-ro 260beon-gil, Daejeong-eup Seogwipo-si, Jeju-do, Republic of Korea 63644. chaeunkim2026@gmail.com
Research conducted at: Sungkyunkwan University N-Center, 2066 Seobu-ro, Jangan-gu, Suwon-si, Gyeonggi-do, Republic of Korea 16419.

https://doi.org/10.64336/001c.160891

1. Introduction

A majority of primary malignant brain tumors are glioblastomas (GBM). GBM is classified as a grade 4 glioma on a scale from 1 to 4 by WHO, upon recognition of its aggressive molecular and histological features (1,2). Though it represents 50.1% of all primary malignant brain tumors, merely 6.9% of patients with GBM exhibit a five-year survival rate and < 1% survive for 10 years or more, making it one of the most fatal neoplasms (3,4).

One contributing factor to these poor outcomes is GBM's uniquely extensive vascular abnormalities. It has long been acknowledged that tumors engage in chronic and compulsory attempts to form new blood vessels to obtain sufficient oxygen and nutrient supply since pre-existing blood vessels are incapable of providing ample resources for their sustainment and expansion. This process is termed angiogenesis, the formation of new blood vessels from preexisting ones. Yet, GBM also utilizes other methods such as the development and fusing of transluminal tissue pillars in a process known as intussusceptive angiogenesis and vascular mimicry, the creation of vessel-like structures by tumor cells (5).

As a result of these processes, GBM demonstrates aberrant blood vessel formation, with fenestrated and diluted walls as well as irregular patterns of endothelium. The inefficient perfusion of these vascular structures contributes to persistent regional hypoxia, despite the fact that their formation is initially driven by hypoxic conditions. This paradoxical cycle promotes an immunosuppressive microenvironment and contributes to therapeutic resistance in glioblastoma.(6,7). Furthermore, the dysregulation of blood vessels models a pathway environment favorable for cancer cell invasion, facilitating rapid tumor growth (8). These biochemical interconnections are reflected in patient prognoses as well, with microvessel density and count as viable prognostic indicators of postoperative survival of patients (9). Taken together, these vascular abnormalities likely contribute to tumor expansion, underscoring the need for a more detailed understanding of the structural alterations in tumor-associated vasculature. In other words, the development of more effective therapeutic strategies for glioblastoma may benefit from targeting its vascular network, with improved characterization of tumor-associated vascular architecture serving as an important prerequisite.

Recognizing the need for further investigation into glioblastoma-associated vascular remodeling and its consequences, we present a single-sample exploratory case study that outlines a reproducible imaging-based workflow to inform future studies with adequate biological replication. This is particularly valuable given the well-documented lack of standardization in immunohistochemical studies across the current literature. (10,11). As a response, we offer a standardized protocol for imaging-based studies that employs immunohistochemistry and confocal microscopy to examine the vasculature of brain tumors. We explore the structural changes of blood vessels caused by GBM by measuring various vascular parameters such as number of branches and junctions, and the maximum and average branch lengths using Fiji(ImageJ)

software, exemplifying the full extent of the morphological alterations in the inner tumoral region and the peritumoral zone surrounding the tumor. Our observations are consistent with prior reports that cerebral vasculature undergoes substantial remodeling in glioblastoma, including increases in branching and ramification.

2. Case study design

This section outlines the standardized procedure for analyzing murine glioblastoma samples by visualizing individual cell nuclei and various vascular characteristics. In this case study, we utilized four brain samples previously generated through glioblastoma (GBM) modeling, following the protocol described by Yei et al. (2025), and did not directly perform the procedures outlined in subsection 2.1(12). In Yei et al. (2025), all animal experimental procedures were approved by the Animal Care and Use Committee (IACUC) of Sungkyunkwan University (SKKUIACUC 2023-08-37-1). In addition, inferential statistical analysis as outlined in subsection 2.6 was not performed (with the exception of cross-tabulation in Figure 6), as the study is based on a single murine brain slice (n = 1). Instead, mean values were calculated across segmented tiles to provide descriptive reference in relation to prior literature. Importantly, tile-level measurements do not represent independent biological replicates and were used solely for within-sample spatial characterization.

2.1 Mouse modeling and brain acquisition

The procedures described in this subsection were conducted previously as part of the study by Yei et al. (2025) and were not performed as part of the present investigation. Figure 1 presents the workflow described in sections 2.1 through 2.4.

Glioblastoma was induced in the right hemisphere of 4 male 22-24 g eight-week-old male C57BL/6N mice with the glioma line of GL261. Each mouse was positioned in the stereotaxic device with the tooth bar and ear bars firmly secured after deep anesthesia and shaving of the head. Following the lubrication of each mouse's eyes to prevent drying, the scalp was cut open to expose the brain, and GL261 was injected in the right hemisphere. The injection site was medial-lateral 1 mm, anterior-posterior -1 mm, and dorsal-ventral 1 mm with 1.5 μl of tumor cell suspension (10^8 cells/mL) at 250 nl/min. Povidone-iodine was administered on the incision subsequently to avoid inflammation. The mice were bred for two additional weeks to allow for the proliferation of tumor cells. The four mice were sacrificed through intracardiac perfusion with saline and ice-cold 4% para-formaldehyde for tissue fixation. Brains were retrieved carefully by removing the skin and the skull to minimize damage to the tissue, then equilibrated and incubated at 4 ^{o}C in ice-cold 4% para-formaldehyde overnight. Before sectioning, the brains were washed with phosphate-buffered saline 3 times at 10-minute intervals.

2.2 Sectioning

The olfactory bulb and the end of the cerebral cortex were sliced off for perpendicular positioning of the longitudinal fissure to the specimen disc surface. Once the disc with the brain affixed by instant adhesive was attached to the buffer tray, it was filled with phosphate-

buffered saline and surrounded with ice. The brain was sliced coronally at the speed of 0.30 mm/s with each slice being 100 μm thick using a Leica VT1200 S. Four brain slices were obtained from each biological replicate, and one of each was chosen for confocal imaging.

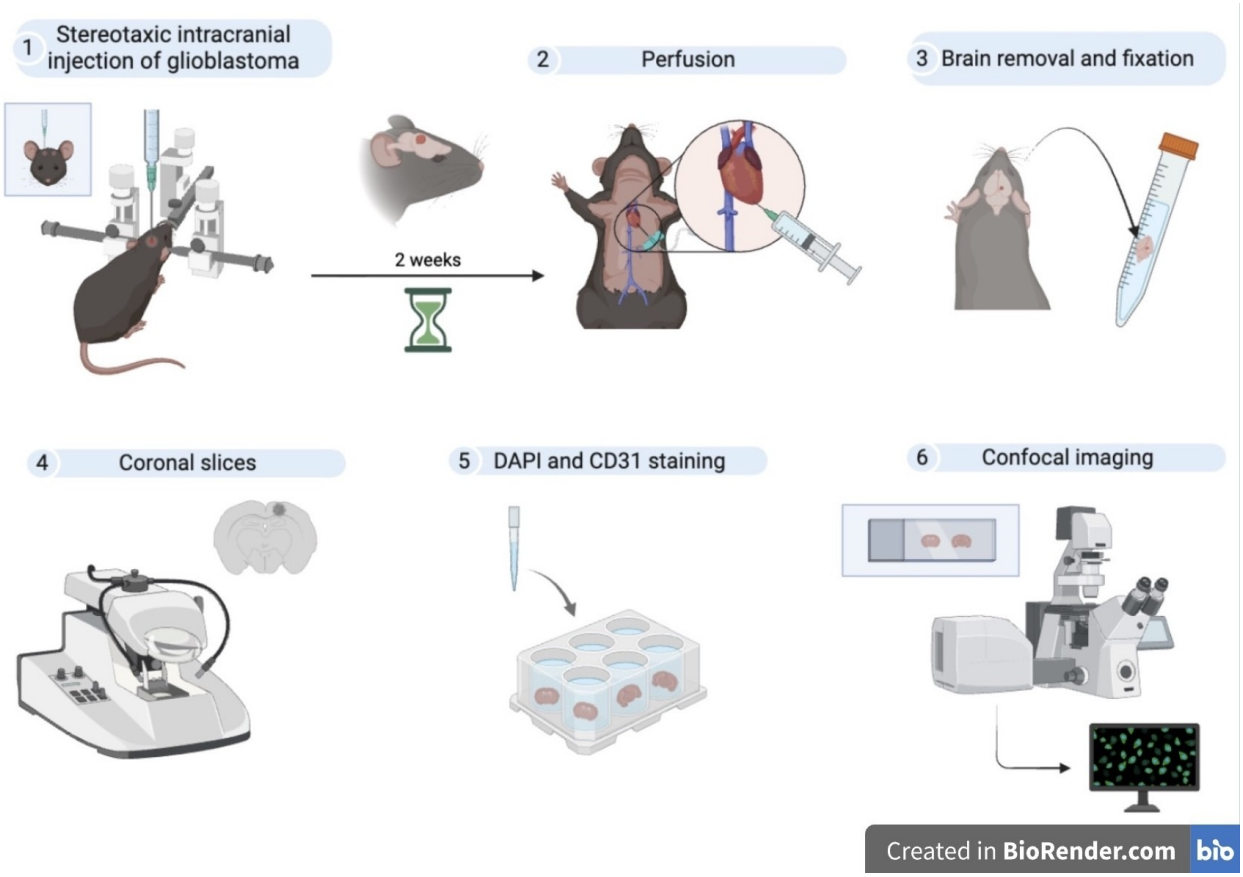

Figure 1. Summary of Materials and Methods
Stereotaxic injection of glioma model GL261 into the right hemisphere of the mouse cortex, followed by perfusion, brain removal, and fixation. The preserved brain was sliced coronally by a vibratome (Leica VT1200 S), then CD31 immunohistochemistry was performed before DAPI counterstaining. After mounting, the brain slices were imaged through confocal microscopy (Leica TCS SP8).

2.3 Staining and mounting

Immunohistochemistry was performed with CD31/PECAM-1 (Platelet Endothelial Cell Adhesion Molecule 1) antibodies. The samples underwent the processes of permeabilization, blocking, and primary antibody incubation with Goat Anti-Human/Mouse/Rat CD31/PECAM-1 Antigen Affinity-purified Polyclonal Antibody at 10 μg/mL for 3 hours at room temperature. Secondary antibody incubation was conducted with NorthernLights™ 493-conjugated Anti-Goat IgG Secondary Antibody. The nuclei of the cells were then counterstained with DAPI (4’,6-diamidino-2-phenylindole). Once staining was complete, the samples were mounted on slides with single drop dispensations of mounting

medium (VECTASHIELD® Hardset™ Antifade Mounting Medium). Coverslips were carefully held at a 45-degree angle and slowly brought down, allowing the medium to spread out beneath them. Once dried, transparent nail polish was applied to their edges to seal the samples and prevent any introduction of impurities.

2.4 Confocal microscopy

With the ipsilateral cortex, the image metrics on the confocal microscope (Leica TCS SP8) were 1624 μm (2853 pixels) for width, 1627 μm (2859 pixels) for height, and 22 μm for depth with 40 slices. X/Y resolution was 1.7571 pixels/μm, voxel size was 0.569 x 0.569 x 0.559 μm^3, and magnification was 0.25. With the contralateral cortex, the image metrics were 1623 μm (2852 pixels) for width, 1625 μm (2856 pixels) for height, and 22 μm for depth with 39 slices. X/Y resolution was 1.7571 pixels/μm, voxel size was 0.569 x 0.569 x 0.559 μm^3, and magnification was 0.25.

2.5 Image analysis

A Z-stack of 39 slices was created for the contralateral hemisphere and another Z-stack of 40 slices was created for the ipsilateral hemisphere. Out of the four sets of brain slice images obtained from confocal microscopy, only one was selected for image analysis, and its Z-stacks were analyzed with Fiji (ImageJ) software (Figure 2A, 2B). Each Z-stack was processed by projecting 'Maximum Intensity' for optimal visualization of each cell. For tile-level analysis, we segmented the confocal image into 29 tiles and distributed the 29 tiles of the ipsilateral image into two groups of 'Peritumoral zone' (Tile #s: 1-14) and 'Inside Tumor' (Tile #s: 15-29) zones, while the tiles from the contralateral image were not grouped separately. In particular, the peritumoral zone was defined based on distinct changes in nuclear density and nuclei distribution as well as an exact distance of 600 μm from the established tumor boundary. Hence, the three areas of comparison are the contralateral hemisphere, which was unaffected by metastasis, the peritumoral brain zone, and the inner tumoral region. For each stains of DAPI and CD31 antibody, the tiles were binarized through appropriate and normalized threshold setting, and their % areas were quantified. Furthermore, through the skeletonization plug-in function in Fiji(ImageJ) software, images stained with CD31 antibody were skeletonized for the quantification of the number of branches, the number of end-point voxels, the number of slab voxels, maximum branch length, average branch length, and the number of triple points. Before quantification for unskeletonized CD31 antibody-stained images, extraneous spots were eliminated through manual despeckling, and for skeletonized images, vasculature that became disconnected through auto-skeletonization was re-attached, both through the 'Paintbrush' function on Fiji (ImageJ) software.

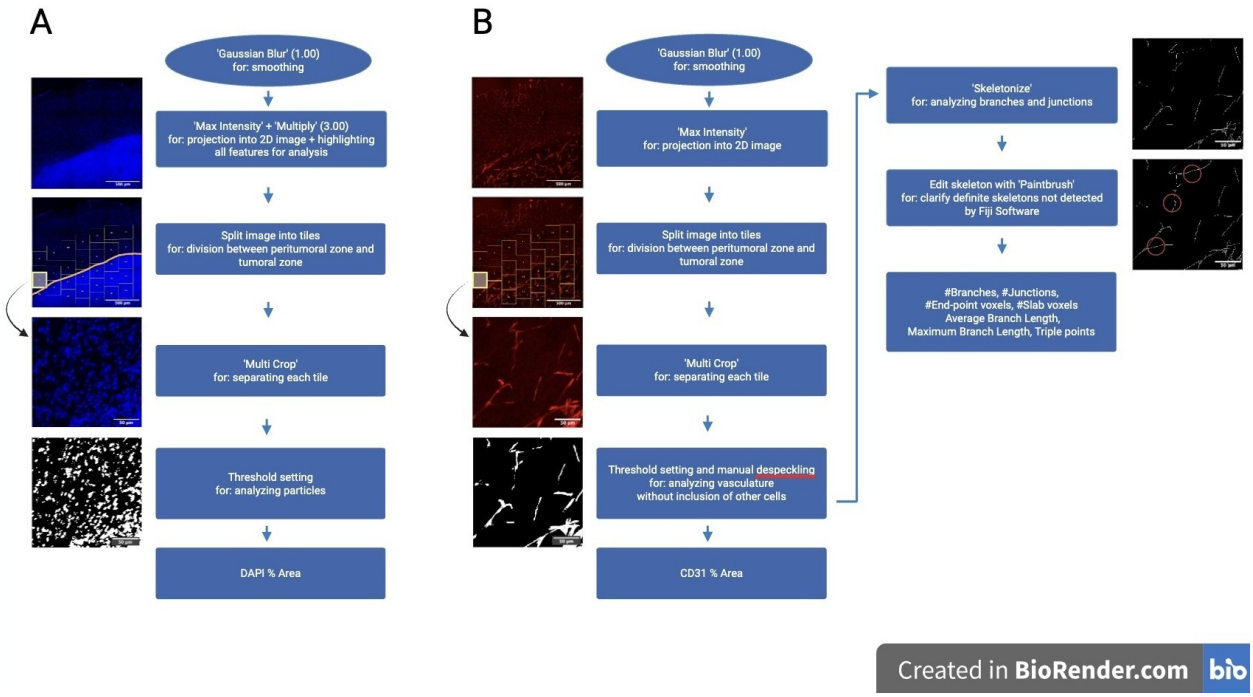

Figure 2. Flowchart of image analysis through Fiji (ImageJ) software
(A) Flowchart of Fiji (ImageJ) software analysis for quantifying % area of DAPI staining. **(B)** Flowchart of Fiji (ImageJ) software analysis for quantifying % area of CD31 staining and skeleton parameters such as number of branches and junctions.

2.6 Statistical procedures for future scaled studies

Because the present study is based on a single biological sample (n = 1), inferential statistical analysis was not performed. The following procedures outline an analytical framework that could be applied in future studies with appropriate biological replication and statistical power.

In such studies, distributional assumptions would first be evaluated using the Shapiro–Wilk test for normality. For variables consistent with normal distributions, group-level comparisons could be conducted using one-way analysis of variance (ANOVA), whereas non-normally distributed variables would be analyzed using the Kruskal–Wallis test. For parameters analyzed using ANOVA, homogeneity of variances would be assessed using Levene's test. In cases where equal variances are not assumed, post hoc comparisons could be performed using Dunnett's T3 test, while Scheffé's test could be applied when variance homogeneity is satisfied.

For the quantification of DAPI-positive area fractions and CD31-positive area fractions, similar procedures could be applied, with normality and variance assumptions evaluated prior to selecting the appropriate parametric or nonparametric test. For categorical analyses

such as the distribution of junction types, cross-tabulation approaches could be used to summarize frequency distributions across regions. For vascular structural parameters derived from skeletonized images (e.g., number of branches, endpoint voxels), nonparametric approaches such as the Kruskal–Wallis test could be employed where distributional assumptions are not met, followed by appropriate post hoc analyses (e.g., Dunn's test) for pairwise comparisons.

Importantly, in all cases, biological replicates—not tile-level segmentations—would constitute the unit of statistical inference. Tile-level measurements may be used for within-sample spatial characterization but would not be treated as independent observations for inferential testing.

3. Sample findings

3.1 Visualization of the glioblastoma mass

The glioblastoma model injected into the cortex of the right hemisphere was highly invasive, as evidenced by its wide-spread incursion of the isocortex (Figure 3A, 3B). Even without the aid of further magnification, this is illustrative of GBM's notorious reputation for its aggressive growth and rapid adaptation to its microenvironment. The GBM's irregular tissue pattern and intense density of cells set it clearly apart from the rest of the brain, enabling obvious detection (Figure 3C).

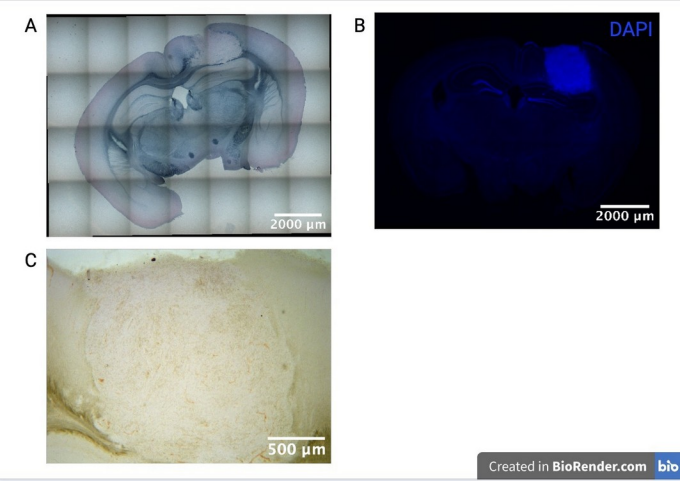

Figure 3. Brightfield and fluorescent images of brain slices with GBM
(A) Whole brain brightfield image of GBM mouse. **(B)** Whole brain fluorescent image of GBM mouse. Red fluorescent color portrays individual cells. **(C)** Magnified brightfield image of GBM illustrates its visible distinction from surrounding parenchyma.

3.2 Tumor identification through DAPI Staining

To confirm the tumor's presence, DAPI counterstaining was performed, following the CD31 immunohistochemistry protocol. DAPI is a frequently-used fluorescent stain employed for

cell counting as it is an effective stainer of cell nuclei, more specifically, the minor grooves of the A-T sequences of DNA (13). Through confocal imaging, we found the tumor cells to reflect a vivid fluorescent chroma of blue compared to its contralateral counterpart (Figure 4A). Subsequent Fiji (ImageJ) analysis measured the % area of DAPI stained portions in each of the tiles and summed up the data for each group to yield respective average values (Figure 4B). Conclusively, we found that the tumoral zone displayed higher mean values of the % area of DAPI compared to the contralateral cortex of the GBM and the peritumoral brain zone. The overwhelmingly high proportion of cells in the tumoral zone signified unregulated increase of tumor cell density in comparison to unaffected or peritumoral cells, reaffirming the defining characteristic of a tumor.

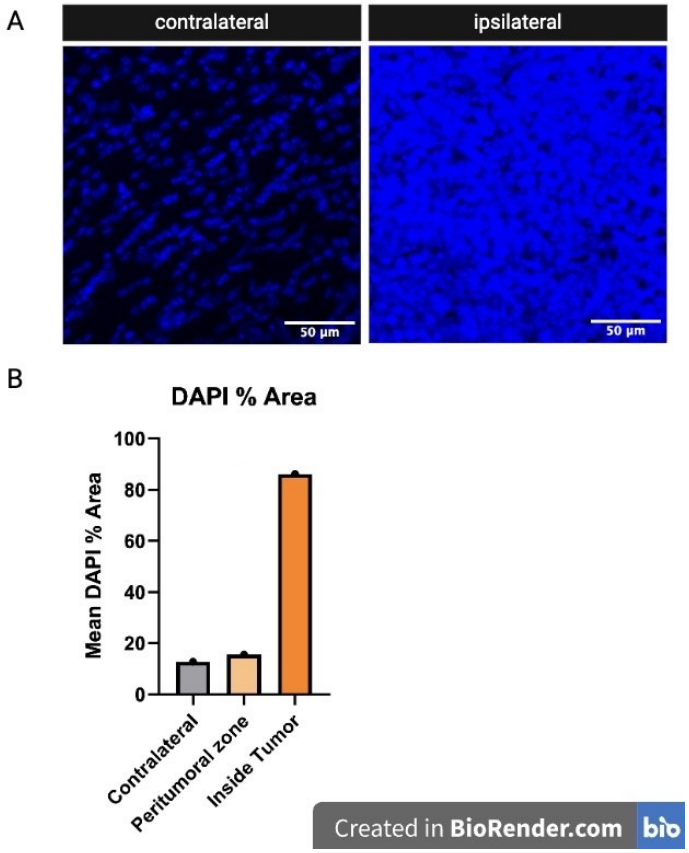

Figure 4. Analysis of DAPI % area
(A) Visual comparison of DAPI stained confocal images of contralateral and ipsilateral hemispheres (Inside Tumor) demonstrate visibly higher density of individual cells in the latter. **(B)** Quantification and comparison of average DAPI % area of the tiles in each of the three groups (n = 1).

3.3 Morphological changes of cerebral vasculature

3.3.1 *CD31 % area*

For deeper insight on the morphological changes of cerebral vasculature due to the inhabitation of GBM, we stained CD31 proteins expressed on the surface of endothelial cells, which align in a cylindrical structure to form blood vessels. Confocal imaging showed large parts of the vasculature to be excessively fenestrated and diluted, with irregular variations in its formation that suggested aggressive angiogenesis (Figure 5A). In addition, the % area of CD31+ regions as a part of each tile, identified by their red fluorescent coloration, was measured and added amongst the three groups (Contralateral, Peritumoral zone, Inside Tumor), then ultimately averaged for comparison (Figure 5C). Our results revealed the highest CD31+ area fraction to be inside the tumoral zone, then the contralateral region, and lastly, the peritumoral brain zone.

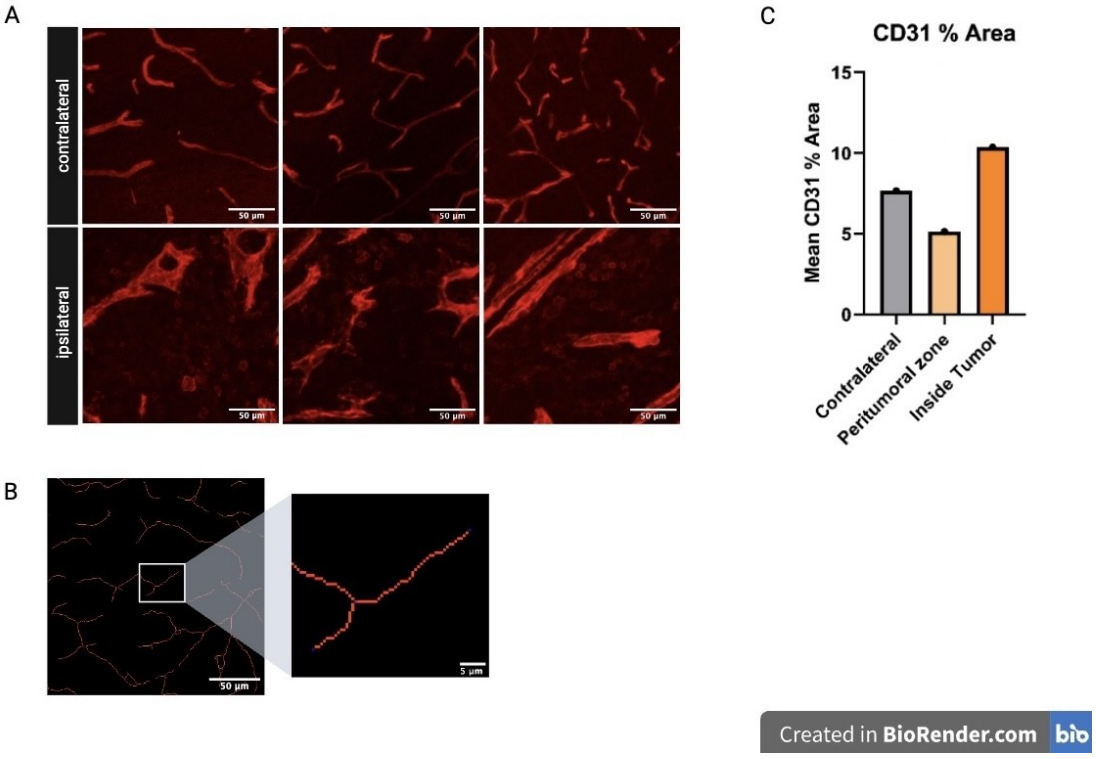

Figure 5. Analysis of CD31 % area

(A) Visual comparison DAPI stained confocal images of contralateral and ipsilateral hemispheres (Inside Tumor) demonstrate visibly abnormal vascular structures in the latter. **(B)** Traced skeleton image of CD31 vasculature; enlarged image of a tip of a branch. Purple pixel represents junction, blue pixels represent end-points, and orange pixels show branch tracing. **(C)** Quantification and comparison of average CD31 % area of the tiles in each of the three groups (n = 1).

3.3.2 *Proportion of junction types*

Next, we aimed to deduce how the frequency of branching varied between each group, categorized by the number of junctions each branch of vasculature possessed. Junctions in Fiji (ImageJ) are characterized by an accumulation of dots corresponding to a bifurcation, obtained through the plugin function of skeletonization (14). We subdivided the number of junctions per branch into three classes: 'Junction 1' denotes exactly 1 junction per branch (Figure 5B); 'Junction 2' indicates 2 junctions per branch; lastly, 'Junction 3' signifies 3 or more junctions per branch. Even though Junction 3 was the most common type while Junction 2 was the least common across all three groups, the contrast was most dramatic for the tumoral zone (Figure 6). More specifically, a majority of branches in the tumoral zone exhibited Junction 3 while Junction 2 partook only about half the proportion relative to its distribution in the contralateral hemisphere and the peritumoral brain zone.

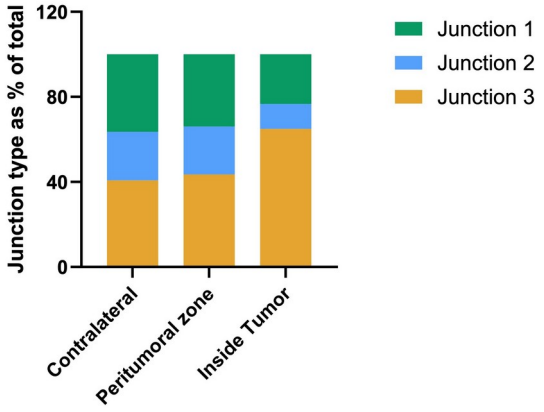

Figure 6. Proportion of junction types within groups

Number of junctions per branch in each of the three groups (n = 1) represented as proportions for comparison. Contralateral: Junction 1 = 36.5%, Junction 2 = 22.7%, Junction 3 = 40.8%; Peritumoral zone: Junction 1 = 33.9%, Junction 2 = 22.6%, Junction 3 = 43.5%; Inside Tumor: Junction 1 = 23.4%, Junction 2 = 11.7%, Junction 3 = 64.9%.

3.3.3 *Analysis of skeletonized CD31 stained images*

To further unravel the morphological changes of vasculature induced by GBM, various parameters were quantified and juxtaposed between the three groups. First, the number of branches per identified skeleton was evaluated and determined to be higher for the inner tumor region compared to the contralateral region (Figure 7A). The number of end-point voxels, which are defined as the number of voxels that have a single neighboring pixel, also demonstrated a higher value for the tumoral zone in comparison with the contralateral region (Figure 7B). The number of pixels between junction-to-junction or junction-endpoint, known as 'slab voxels', was calculated to demonstrate the highest average count for the

inside tumor region, followed by the contralateral, then the peritumoral zones (Figure 7C). Average and maximum branch lengths were quantified to be in decreasing order of contralateral hemisphere, peritumoral brain zone, then inner tumoral region (Figure 7D, 7E). Finally, triple points, which can be classified as primary branching points, as Cribaro et al. (2021) have previously described as y- or t-shaped bifurcations, were most prevalent inside the tumoral zone even when juxtaposed with the peritumoral zone (Figure 7F) (15).

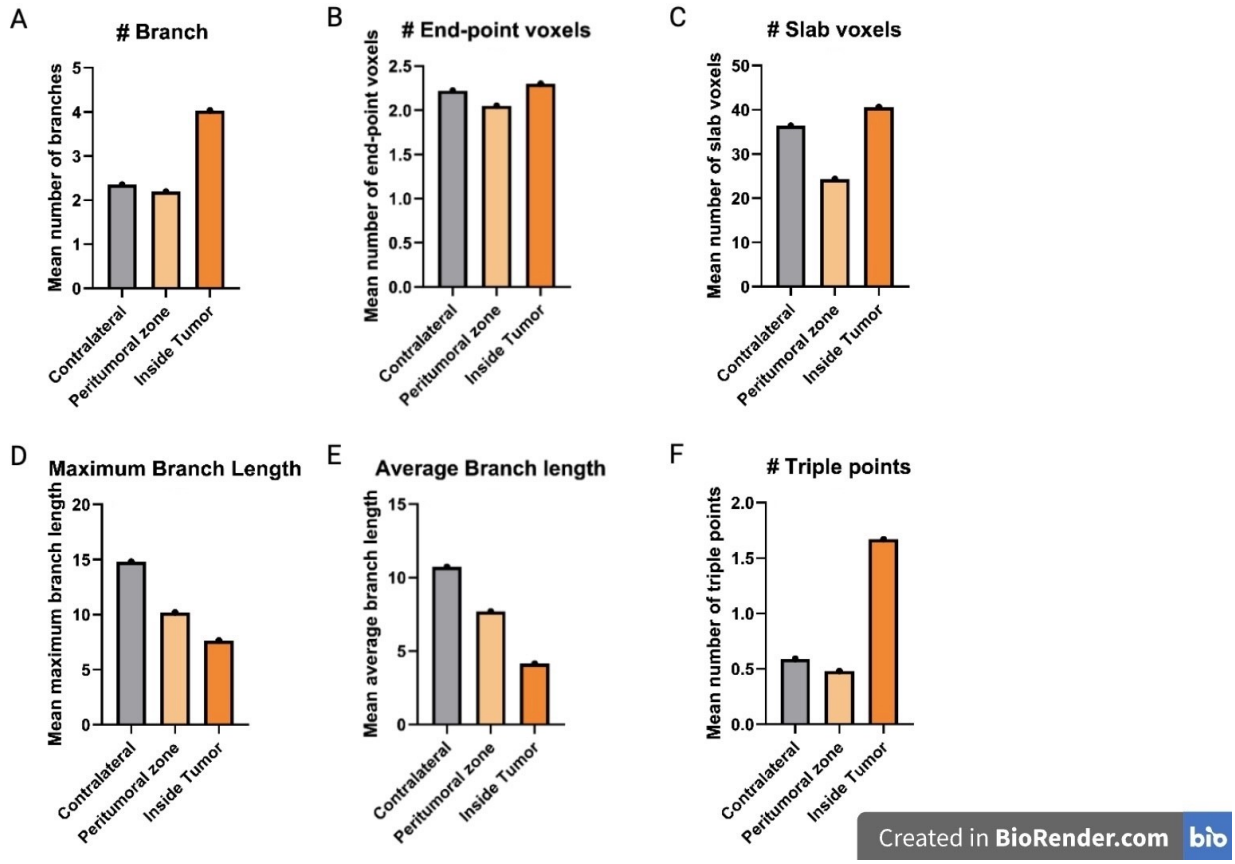

Figure 7. Analysis of skeletonized CD31 stained images
(A) Quantification and comparison of the number of branches per identified skeleton in each of the three groups (n = 1). **(B)** Quantification and comparison of the number of end-point voxels in each of the three groups (n = 1). **(C)** Quantification and comparison of the number of slab voxels in each of the three groups (n = 1). **(D)** Quantification and comparison of the average branch length in each of the three groups (n = 1). **(E)** Quantification and comparison of the maximum branch length in each of the three groups (n = 1). **(F)** Quantification and comparison of the number of triple points in each of the three groups (n = 1).

4. Discussion

In this study, to understand how the aggressive brain tumor, glioblastoma (GBM), induces severe variations in cerebral vasculature, we analyzed confocal images of the ipsilateral and contralateral hemispheres from mouse brain

tissues administered with glioma samples. Our descriptive analysis demonstrated that the tumor vasculature has a larger vascular area ratio compared to the contralateral zone (6). This pattern observed in this case study is consistent with the GBM endothelium's display of increased volumetric surface in relation to high rates of division, measured by the Ki67 Index (15). The small scale of the difference between the CD31+ area fraction of intratumor vessels and contralateral vessels raises the possibility of the compression of their own vessels due to the increased cellular density and solid stress, potentially inducing vessel collapses and diminished abilities (16). Similarly, the decrease of CD31 % area in the peritumoral zone compared to the tumor mass may be understood in the context of solid stress, derived from the structural factors within the tumor's environment, such as increased density of cancer cells (17). According to Stylianopoulos et al. (2013), solid stress applied to the outer parenchymal tissue is associated with an elliptical compression of peritumoral blood vessels (18). This is especially noteworthy in that solid stress generated by brain tumor causally impairs neurological functions in patients, which is one of the most detrimental clinical symptoms of GBM (19).

The findings from skeletonized vessels and the high proportion of Junction type 3 as shown in Figures 6 and 7 may be related to the six types of neovascularization: angiogenesis, intussusceptive angiogenesis, vasculogenesis, vascular co-option, vascular mimicry, and the transdifferentiation of cancer stem cells (CSCs) (5,20). For example, the high number of dead-ends and vascular tip irregularities of glioblastomas are generally attributed to the disorganized and dysfunctional aspect of tumor vasculature induced by aberrant angiogenesis following vessel co-option, especially since the sprouting of angiogenesis is initiated with angiopoietin-mediated breakdown of preexisting vessels (21). While current literature affirms that vasculogenesis, and CSC differentiation/incorporation all contribute to vascular elongation, a human GBM patient study conducted by Radbruch et al. (2014), does imply that extensive neovascularization is not limited to longer blood vessels since the unstable nature of the rapidly conjured vasculature prevents such developments (22). The formation of primary branching points as means of GBM neovascularization strategy, represented in our study through triple points, may be associated with angiogenesis and intussusceptive angiogenesis (15).

On that note, we suggest that further studies be conducted especially on how these morphological changes lead to different patient prognoses and symptoms for a more directed focus on treatment methods. One specific direction for future research is the evaluation of vascular network topology using quantitative descriptors such as junction-order distributions and aggregate measures of branching complexity. In our current study, we operationalized branching structure using skeletonized vascular graphs, where branching points correspond to junctions, vessel segments to branches, and junction-order distribution was categorized by the number of junctions per branch. Within this framework, the intratumoral region in this specimen exhibited a higher relative frequency of higher-degree nodes

compared to surrounding regions, suggesting increased local branching complexity. While this pattern is consistent with prior descriptions of disorganized tumor vasculature, the present single-sample design and the use of semi-manual image processing steps preclude quantitative statistical analysis, assessment of reproducibility, sensitivity to preprocessing parameters, or association with biological or clinical outcomes. Accordingly, these topological features should be interpreted strictly as descriptive characteristics of this specimen. Future studies incorporating multiple biological replicates, fully standardized segmentation pipelines, and outcome-linked datasets would be required to perhaps produce a quantitative network-based metrics based on this categorization and determine whether they hold potential as candidate biomarkers of tumor behavior and determinants of treatment selection. Moreover, we strongly recommend exploring all the ways in which numerous types of neovascularization impact the proliferation of GBM, in a way that is not limited to angiogenesis as other neovascularization methods are also key players in its proliferation (23).

One limitation of this study was the implementation of manual despeckling and attachment through the 'Paintbrush' function on Fiji (ImageJ) software. Though initially purposed to reduce error by removing irrelevant stains and re-connecting visible vasculature that became segmented through automatized skeletonization, the two processes may have contributed to some human bias. For CD31-stained tiles, the target for stain removal was restricted to annular single cells that were visually distinct from surrounding vascular structures. The proportion of pixels altered during this process was low in absolute terms (contralateral: 0.10 ± 0.05%, peritumoral: 0.11 ± 0.18%, intratumoral: 3.18 ± 0.21%), based on ~20% of randomly selected tiles, although relative variability was higher in regions with very small mean values.

For skeletonized images, reconnection was limited to segments that were visibly continuous but became artificially disconnected during binary reconstruction in Fiji (ImageJ). The proportion of pixels altered during this step was larger (contralateral: 11 ± 9%, peritumoral: 15.7 ± 5.0%, intratumoral: 5.0 ± 5.0%), based on ~20% of randomly selected tiles, reflecting the extent of manual correction required to address false negatives introduced during skeletonization. These modifications, particularly in the contralateral and peritumoral regions, exhibit substantial variability and may influence derived topological features.

Accordingly, while these procedures were implemented to improve structural continuity and reduce segmentation artifacts, the potential impact of manual intervention on quantitative vascular metrics cannot be excluded and should be considered when interpreting the results.

Another limitation is that because this is a case study relying on Z stacks of a single brain slice and statistical analysis cannot be performed with n = 1, we cannot reliably validate the difference between real effect and random chance, which has the possibility of leading to flawed conclusions. In light of this concern, we have minimized the number of inferential claims in

this paper to avoid the exaggerations of interpretations. It is one of the main objectives of this paper to outline the specific methodologies of the research process in investigating the vasculature of glioblastoma; thus, with greater sample size and biological replicates, future studies can reference this study's procedures to statistically confirm the sample findings provided.

5. Conclusion

Blood vessels play a crucial role in the proliferation of glioblastoma. Therein, a better understanding of its vascular changes through a more standardized set of procedures in immunohistochemistry, confocal imaging, as well as subsequent image and statistical analysis is imperative for the fight against it through clinical therapies. In this investigation, we examined a single murine brain slice to produce a methodological case study on how GBM causes morphological changes to cerebral vasculature in areas of vascular area ratio, number of branches and junctions, number of end-point and slab voxels, average and maximum branch lengths, and triple points. Overall, our data is in line with previous observations regarding tumoral vascular characteristics, particularly the presence of neovascularization, suggesting that the presented methodology is effective and accurate. Further research is necessary to investigate GBM's predominant neovascularization strategies, which could serve as key targets for future treatment modalities.

Acknowledgements

The author would like to thank Dr. Minah Suh and Seong-Eun Ryu from the Department of Biomedical Engineering, Sungkyunkwan University for their mentorship throughout the research process.

6. References

1. Louis, D. N., Perry, A., Reifenberger, G., von Deimling, A., Figarella-Branger, D., Cavenee, W. K., et al. (2016). The 2016 World Health Organization Classification of Tumors of the Central Nervous System: a summary. *Acta Neuropathol*, *131*(6), 803–820. https://doi.org/10.1007/s00401-016-1545-1

2. Ferris, S. P., Hofmann, J. W., Solomon, D. A., Perry, A. (2017). Characterization of gliomas: from morphology to molecules. *Virchows Arch*, *471*(2), 257–269. https://doi.org/10.1007/s00428-017-2181-4

3. Ostrom, Q. T., Price, M., Neff, C., Cioffi, G., Waite, K. A., Kruchko, C., et al. (2022). CBTRUS Statistical Report: Primary Brain and Other Central Nervous System Tumors Diagnosed in the United States in 2015-2019. *Neuro Oncol*, *24*(Suppl 5), v1–v95. https://doi.org/10.1093/neuonc/noac202

4. Tykocki, T., Eltayeb, M. (2018). Ten-year survival in glioblastoma. A systematic review. *J Clin Neurosci*, *54*, 7–13. https://doi.org/10.1016/j.jocn.2018.05.002

5. Lugano, R., Ramachandran, M., Dimberg, A. (2020). Tumor angiogenesis: causes, consequences, challenges and opportunities. *Cell Mol Life Sci*, *77*(9), 1745–1770. https://doi.org/10.1007/s00018-019-03351-7

6. Gerstner, E. R., Emblem, K. E., Yen, Y. F., Dietrich, J., Jordan, J. T., Catana, C., et al. (2020). Vascular dysfunction promotes regional hypoxia after bevacizumab therapy in recurrent glioblastoma patients. *Neurooncol Adv*, *2*(1), vdaa157. https://doi.org/10.1093/noajnl/vdaa157

7. Huang, W. J., Chen, W. W., Zhang, X. (2016). Glioblastoma multiforme: Effect of hypoxia and hypoxia inducible factors on therapeutic approaches. *Oncol Lett*, *12*(4), 2283–2288. https://doi.org/10.3892/ol.2016.4952

8. Scheer, K. G., Ebert, L. M., Samuel, M. S., Bonder, C. S., Gomez, G. A. (2023). Bevacizumab-Induced Hypertension in Glioblastoma Patients and Its Potential as a Modulator of Treatment Response. *Hypertension*, *80*(8), 1590–1597. https://doi.org/10.1161/HYPERTENSIONAHA.123.21119

9. Leon, S. P., Folkerth, R. D., Black, P. M. (1996). Microvessel density is a prognostic indicator for patients with astroglial brain tumors. *Cancer*, *77*(2), 362–372. https://doi.org/10.1002/(SICI)1097-0142(19960115)77:2<362::AID-CNCR20>3.0.CO;2-Z

10. Fedchenko, N., Reifenrath, J. (2014). Different approaches for interpretation and reporting of immunohistochemistry analysis results in the bone tissue - a review. Diagn Pathol, 9, 221. https://doi.org/10.1186/s13000-014-0221-9

11. Mebratie, D. Y., Dagnaw, G. G. (2024). Review of immunohistochemistry techniques: Applications, current status, and future perspectives. Semin Diagn Pathol, 41(3), 154–160. https://doi.org/10.1053/j.semdp.2024.05.001

12. Yei, J., Lee, N. K., Ryu, S., Ryu, S. E., Lee, J., Park, T., et al. (2025). Glioma-Associated Microglia Potentiate Neuronal Hyper-Excitability in the Glioma Environment. *Neuro Oncol*. https://doi.org/10.1093/neuonc/noaf181

13. Kapuscinski, J. (1995). DAPI: a DNA-specific fluorescent probe. *Biotech Histochem*, *70*(5), 220–233. https://doi.org/10.3109/10520299509108199

14. Carpentier, G., Berndt, S., Ferratge, S., Rasband, W., Cuendet, M., Uzan, G., et al. (2020). Angiogenesis Analyzer for ImageJ - A comparative morphometric analysis of "Endothelial Tube Formation Assay" and "Fibrin Bead Assay". *Sci Rep*, *10*(1), 11568. https://doi.org/10.1038/s41598-020-67289-8

15. Cribaro, G. P., Saavedra-Lopez, E., Romarate, L., Mitxitorena, I., Diaz, L. R., Casanova, P. V., et al. (2021). Three-dimensional vascular microenvironment landscape in human glioblastoma. *Acta Neuropathol Commun*, *9*(1), 24. https://doi.org/10.1186/s40478-020-01115-0

16. Padera, T. P., Stoll, B. R., Tooredman, J. B., Capen, D., di Tomaso, E., Jain, R. K. (2004). Pathology: cancer cells compress intratumour vessels. *Nature*, *427*(6976), 695. https://doi.org/10.1038/427695a

17. Kalli, M., Stylianopoulos, T. (2018). Defining the Role of Solid Stress and Matrix Stiffness in Cancer Cell Proliferation and Metastasis. *Front Oncol*, *8*, 55. https://doi.org/10.3389/fonc.2018.00055

18. Stylianopoulos, T., Martin, J. D., Snuderl, M., Mpekris, F., Jain, S. R., Jain, R. K. (2013). Coevolution of solid stress and interstitial fluid pressure in tumors during progression: implications for vascular collapse. *Cancer Res*, *73*(13), 3833–3841. https://doi.org/10.1158/0008-5472.CAN-12-4521

19. Seano, G., Nia, H. T., Emblem, K. E., Datta, M., Ren, J., Krishnan, S., et al. (2019). Solid stress in brain tumours causes neuronal loss and neurological dysfunction and can be reversed by lithium. *Nat Biomed Eng*, *3*(3), 230–245. https://doi.org/10.1038/s41551-018-0334-7

20. Ghoochani, A., Yakubov, E., Sehm, T., Fan, Z., Hock, S., Buchfelder, M., et al. (2016). A versatile ex vivo technique for assaying tumor angiogenesis and microglia in the brain. *Oncotarget*, *7*(2), 1838–1853. https://doi.org/10.18632/oncotarget.6550

21. Hardee, M. E., Zagzag, D. (2012). Mechanisms of glioma-associated neovascularization. *Am J Pathol*, *181*(4), 1126–1141. https://doi.org/10.1016/j.ajpath.2012.06.030

22. Radbruch, A., Eidel, O., Wiestler, B., Paech, D., Burth, S., Kickingereder, P., et al. (2014). Quantification of tumor vessels in glioblastoma patients using time-of-flight angiography at 7 Tesla: a feasibility study. *PLoS One*, *9*(11), e110727. https://doi.org/10.1371/journal.pone.0110727

23. Beylerli, O., Gareev, I., Musaev, E., Ilyasova, T., Roumiantsev, S., Chekhonin, V. (2025). Angiogenesis and Resistance Mechanisms in Glioblastoma: Targeting Alternative Vascularization Pathways to Overcome Therapy Resistance. *Curr Pharm Des*. https://doi.org/10.2174/0113816128367551250703122830